IDRiM (2026) 16 (2) **ISSN: 2185-8322**
DOI10.5595/001c.173262

Journal of Integrated Disaster Risk Management

Regular Article

Hydrodynamic Flood Modelling and GIS-Based Risk Mapping for Identifying Urbanization-Safe Zones in Hanwella, Sri Lanka

Dilum U. Haththotuwa Gamage[1*], Hasitha Erandi[1], Ikha Magdalena[2] and Sanjeewa Perera[1]

Received: 04/09/2025 / Accepted: 17/08/2026 / Published online: 29/10/2026

Abstract Urban expansion in flood-prone regions increases exposure to hydrological hazards and makes flood-informed land-use planning increasingly important. Hanwella, located in the Kelani River basin of Sri Lanka, is particularly vulnerable to flooding due to intense rainfall, river overflow, and growing urban pressure. This study develops a two-dimensional hydrodynamic flood modelling framework based on the shallow water equations and applies a Godunov-type finite volume method with the Harten–Lax–van Leer (HLL) Riemann solver to simulate water-level dynamics in the Hanwella region. The two-dimensional shallow water equation model explicitly incorporates upstream river contributions together with overland flow contributions from the surrounding river basin to represent the major hydrological inputs. The model integrates hydrological, meteorological, and topographical data obtained from the Sri Lankan Irrigation Department and NASA datasets. Model performance was validated against observed water-level records using the Nash–Sutcliffe Efficiency coefficient, yielding an NSE value of 0.7, which indicates acceptable predictive performance. Uncertainty was examined through validation-residual statistics and a qualitative expert-based discussion of potential uncertainty sources; formal parameter-sensitivity and probabilistic uncertainty-propagation analyses were beyond the scope of this study. The simulated outputs were subsequently integrated with GIS-based spatial analysis using the Flood Inundation Calculator plugin in QGIS to generate flood-risk maps under different rainfall intensities and to identify areas with relatively lower flood susceptibility. The findings provide a practical basis for zoning, risk-sensitive land-use planning, and targeted flood mitigation in the Hanwella region.

Keywords: flood risk modelling, shallow water equations, GIS analysis, hydrodynamic simulation, urban planning

[1] Department of Mathematics, Faculty of Science, University of Colombo, Colombo, Sri Lanka
[2] Faculty of Mathematics and Natural Sciences, Bandung Institute of Technology, Bandung, Indonesia
* Corresponding author email: gamage.dilum126@gmail.com

1. INTRODUCTION

Flood risk assessment and modelling are vital for predicting flood events, enabling early warnings, and supporting disaster preparedness. These assessments have progressed from empirical and statistical methods to advanced numerical simulations that improve the identification of high-risk areas. Accurate modelling supports infrastructure planning, policy development, and resource allocation for mitigation and recovery (Moufar & Perera, 2018). In rapidly urbanizing flood-prone regions, flood modelling also supports land-use planning, zoning, and the identification of areas that are more suitable for future development (Hirabayashi et al., 2021; Jongman et al., 2014). In this study, these areas are termed urbanization-safe zones, referring to locations that remain under comparatively low flood susceptibility across the simulated rainfall scenarios and are therefore considered more suitable for future development, subject to environmental and planning constraints. Such zones are not interpreted as absolutely flood-free areas, but rather as areas with relatively lower modelled flood depth, inundation extent, and exposure under the adopted hydrological conditions (Chen et al., 2022; Global Facility for Disaster Reduction and Recovery, 2017). Flood risk modelling also helps address uncertainties introduced by climate change, where historical data may no longer reliably predict future risks, and can support related planning applications such as insurance and resilience strategies (Hirabayashi et al., 2021; Jongman et al., 2014).

Hydrodynamic models used for flood simulation vary in complexity from one-dimensional (1D) to three-dimensional (3D) formulations, depending on the level of physical detail required. One-dimensional models, such as HEC-RAS and SWMM, represent flow mainly along the channel axis and are computationally efficient, but they provide limited spatial detail for floodplain inundation. In contrast, two-dimensional (2D) models, including LISFLOOD-FP, TUFLOW, and Delft3D, can represent both longitudinal and lateral flow, making them more suitable for simulating flood extent and water depth across river-floodplain systems. For highly complex flow situations, three-dimensional (3D) models such as TELEMAC and FLOW-3D can further resolve vertical velocity structure and detailed flow dynamics, although they require substantially greater computational resources.

The performance of these models also depends on the numerical method used to solve the governing equations. The Finite Difference Method (FDM) approximates derivatives through difference equations and is relatively simple to implement, but it faces stability and accuracy limitations in irregular geometries. The Finite Element Method (FEM) is well suited to complex boundaries because it uses variational principles to minimize approximation errors, although this often comes at a higher computational cost. The Finite Volume Method (FVM), by contrast, conserves fluxes across control volumes and is especially effective in handling discontinuities and rapidly varying flows, which makes it particularly attractive for flood modelling. Its robustness and ability to capture dynamic flood behaviour have been demonstrated in previous studies (Benedini & Tsakiris, 2013; Chen et al., 2021). Among the available approaches, 2D hydrodynamic models solved using FVM are especially appropriate for floodplain studies because they provide a practical balance between physical detail, numerical stability, accuracy, and computational efficiency, while remaining less demanding

than fully 3D simulations (Brunner, 2024; Caviedes-Voullième et al., 2020; Costabile et al., 2021; Kurganov, 2018).

To place the proposed model in context, its improvement in flood prediction accuracy can be interpreted relative to both simpler and more data-intensive counterpart approaches. A practical low-complexity counterpart is the SWAT rainfall-runoff model, which has been applied in Sri Lanka for basin-scale hydrological simulation. For example, in the Kala Oya basin, SWAT achieved calibration and validation NSE values of 0.59 and 0.56, respectively, indicating moderate performance for streamflow simulation (Makumbura et al., 2022; Perera et al., 2024). However, such models are generally less suitable for resolving detailed spatial inundation patterns in urban floodplains because they focus mainly on runoff generation at the basin scale rather than on two-dimensional flood spreading (Iresh et al., 2021). A more advanced but also more demanding counterpart is the combined 1D/2D HEC-RAS hydraulic model, which has been shown in the Lower Kelani River Basin to outperform other hydraulic configurations for predicting flow and inundation. Nevertheless, this approach depends on high-resolution topographic data and a more detailed hydraulic setup, which increases both data requirements and modelling complexity (Samarasinghe, Basnayaka, et al., 2022). In highly urbanized environments, SWMM-based urban drainage modelling is another possible alternative, but it typically requires extensive drainage-network information. For instance, one recent urban flood study used 1168 inlets, 403 manholes, 11.9 km of sewers, and three outfalls, illustrating the level of infrastructure detail often needed for such applications (Barreiro et al., 2022). Therefore, the present model offers a practical compromise: it is more physically informative than simpler rainfall-runoff approaches, while remaining more feasible than heavily data-dependent urban drainage models or fully coupled high-resolution hydraulic simulations in a data-limited study area.

Although two-dimensional shallow water equation-based flood models are widely used in hydrology and hydraulic engineering, their application to planning-oriented flood assessment in Sri Lanka remains limited, particularly in studies that explicitly connect hydrodynamic simulation outputs with the identification of areas suitable for safer urban expansion. While two-dimensional shallow water equation systems implemented through the Finite Volume Method and the Harten–Lax–van Leer (HLL) Riemann solver are not new in themselves, the present study differs in its hydrological and planning-oriented adaptation. In particular, the model explicitly incorporates both upstream river contributions and overland flow contributions from the surrounding basin, allowing flood dynamics in Hanwella to be represented in a more locally relevant manner. The study further integrates local hydrological records from the Kelani basin, DEM-based terrain representation, rainfall-intensity-based flood mapping, and GIS-supported delineation of relatively safe urbanization zones. Runoff is estimated using the SCS Curve Number method, while the continuity and momentum equations govern the combined hydrological inputs within a two-dimensional shallow water equation framework solved using a Godunov-type Finite Volume Method with the HLL Riemann solver (Chow et al., 1988; Elong et al., 2022; Kurganov, 2018; LeVeque & George, 2004).

This study utilizes three main data categories: hydrological data (river parameters and water levels), meteorological data (rainfall), and topographical data (Digital Elevation Models),

sourced from NASA databases and the Sri Lankan Irrigation Department for the period 2000 to 2024. The flood model is applied to the Hanwella catchment of the Kelani River in Colombo District, incorporating field-calibrated parameters. Model performance is assessed using the Nash–Sutcliffe Efficiency (NSE) score and validated against observed data. The methodological framework is grounded in the application of two-dimensional shallow water equations to simulate surface flow dynamics.

The remainder of the paper is organized as follows: key concepts and assumptions of the SCS-CN method, computation of flow rate, development of the numerical model using the shallow water equations, implementation of the Finite Volume Method with the Godunov approach, flux calculations, and finally, the scenario-response analysis and generation of flood risk maps.

2. MODELLING FRAMEWORK AND METHODOLOGY

2.1 Key Concepts and Assumptions

Initial abstraction (I_a) refers to the initial water losses due to interception, surface storage, and infiltration before runoff begins. In the SCS-CN method, I_a is estimated as a function of the soil's storage capacity (S), defined by the relationship:

$$I_a = 0.2S. \tag{1}$$

Where S is the soil's maximum storage capacity, indicating the volume of water that must be absorbed by the surface and soil before contributing to runoff (Chow et al., 1988; U.S. Department of Agriculture, 1986). Maximum runoff ($P_{e(max)}$) is calculated as the difference between total rainfall (P) and initial abstraction (I_a). This value represents the maximum possible runoff if the soil's storage capacity is not fully utilized:

$$P_{e(max)} = P - I_a. \tag{2}$$

Excess rainfall (P_e) is the actual runoff that remains after accounting for the initial abstraction and the portion of rainfall absorbed by the soil (F_a). The amount of water used to fulfill the soil storage is given by:

$$F_a = P - I_a - P_e. \tag{3}$$

The SCS-CN method assumes a proportional relationship between the actual water used to fulfill soil storage and the total available storage, as well as between actual runoff and potential maximum runoff:

$$\frac{F_a}{S} = \frac{P - I_a - P_e}{S} = \frac{P_e}{P - I_a}. \tag{4}$$

This relationship ensures that the actual water distribution between storage and runoff is consistent with the potential maximum values (Chow et al., 1988). The adjusted soil storage

capacity (S) is estimated using the SCS Potential Maximum Retention equation, accounting for soil type and hydrologic conditions:

$$S = \frac{25400}{CN} - 254. \tag{5}$$

The SCS Curve Number (CN) method provides a widely used framework for estimating direct runoff from rainfall events (Chow et al., 1988; U.S. Department of Agriculture, 1986).

$$P_e = \frac{(P-I_a)^2}{P-I_a+S} = \frac{(P-(0.2)S)^2}{(P+(0.8)S)}. \tag{6}$$

Runoff occurs only when $P > I_a$, adhering to a nonlinear relationship between rainfall, runoff, and soil storage. The SCS-CN method is constrained by its empirical nature and the assumptions that $I_a = 0.2S$, and that soil properties are spatially uniform (Chow et al., 1988; U.S. Department of Agriculture, 1986).

2.1.1 Computation of Flow Rate

The channel discharge was estimated using Manning's equation,

$$Q_{Channel} = \frac{1}{n_m} A_s R_H^{2/3} S_0^{1/2}. \tag{7}$$

Where $Q_{channel}$ is the discharge (m^3/s), $n_m$is the Manning's roughness coefficient $(-)$, A is the wetted cross-sectional area (m^2), R_H is the hydraulic radius (m), and $S_0$is the bed slope $(-)$.

2.2 Numerical Model Using Shallow Water Equations

The conservative form of the two-dimensional shallow water equations is derived from the Navier–Stokes equations. These equations conserve mass and momentum while incorporating source terms that account for bottom slope, friction, and external inputs such as rainfall, upstream inflows, and overland contributions (Coulibaly et al., 2020; Elong et al., 2022).

$$\frac{\partial(h)}{\partial t} + \frac{\partial(hu)}{\partial x} + \frac{\partial(hv)}{\partial y} = P + Q_{New} + Q_{Inflow}, \tag{8}$$

$$\frac{\partial(hu)}{\partial t} + \frac{\partial\left(hu^2+\frac{1}{2}gh^2\right)}{\partial x} + \frac{\partial(huv)}{\partial y} = -gh\frac{\partial Z}{\partial x} - (n_m)^2\frac{\sqrt{(u^2+v^2)}}{h^{(4/3)}}u + Q_{Mtm-x}, \tag{9}$$

$$\frac{\partial(hv)}{\partial t} + \frac{\partial(huv)}{\partial x} + \frac{\partial\left(hv^2+\frac{1}{2}gh^2\right)}{\partial y} = -gh\frac{\partial Z}{\partial y} - (n_m)^2\frac{\sqrt{(u^2+v^2)}}{h^{(4/3)}}v + Q_{Mtm-y}. \tag{10}$$

Here, h denotes the water depth, u and v are the depth-averaged velocity components in the x- and y-directions, respectively; g is the gravitational acceleration; Z is the bed elevation. The terms P, Q_{new}, Q_{inflow} represent rainfall input, overland flow contribution, and upstream river inflow contribution, respectively. In addition, Q_{Mtm-x}, Q_{Mtm-y} denote the momentum source terms in the x- and y- directions, respectively. For compactness, the system of shallow water equations can be written in vector form as follows (Coulibaly et al., 2020),

$$\frac{\partial U}{\partial t} + \frac{\partial F(U)}{\partial x} + \frac{\partial G(U)}{\partial y} = S_s + S_f + S_p. \quad (11)$$

Here x and y represent the Cartesian coordinates, t is the time, U is the vector of conservative variables (mass and momentum), $F(U)$ and $G(U)$ are the flux vectors in the x- and y- directions, respectively (Coulibaly et al., 2020). The bottom slope, the friction terms, and the precipitation term are expressed by S_s, S_f and S_p respectively (Elong et al., 2022).

2.2.1 FVM-Godunov Approach

The Finite Volume Method (FVM), combined with the Godunov scheme, offers a reliable approach for solving the 2D shallow water equations. The total source term $S(U)$ is expressed as the sum of slope, friction, and pressure components: $S(U) = S_s + S_f + S_p$. This formulation is applied to each cell and time step for accurate numerical integration (Coulibaly et al., 2020; Elong et al., 2022; Kurganov, 2018; LeVeque & George, 2004).

$$\int_{x_{i-1/2}}^{x_{i+1/2}} \int_{y_{j-1/2}}^{y_{j+1/2}} \int_{t^n}^{t^{n+1}} \left(\frac{\partial U}{\partial t} + \frac{\partial (F(U))}{\partial x} + \frac{\partial (G(U))}{\partial y}\right) dx\, dy\, dt = \int_{x_{i-1/2}}^{x_{i+1/2}} \int_{y_{j-1/2}}^{y_{j+1/2}} \int_{t^n}^{t^{n+1}} S(U)\, dx\, dy\, dt. \quad (12)$$

To solve this equation, it is helpful to break it down into smaller parts by solving it separately along the x- and y-directions (Coulibaly et al., 2020; Elong et al., 2022; Kurganov, 2018). The numerical solution is obtained as follows:

$$U_{i,j}^{n+2/4} = U_{i,j}^{n} - \left(\frac{\Delta t}{\Delta x}\right)\left[F_{i+1/2,j}^{n} - F_{i-1/2,j}^{n}\right] - \left(\frac{\Delta t}{\Delta y}\right)\left[G_{i+1/2,j}^{n+1/4} - G_{i-1/2,j}^{n+1/4}\right]. \quad (13)$$

The source terms are integrated as follows (Coulibaly et al., 2020; Kurganov, 2018):

$$\frac{U_{i,j}^{n+3/4} - U_{i,j}^{n+2/4}}{\Delta t} = S_f\left(U_{i,j}^{n+2/4}\right) + S_s\left(U_{i,j}^{n+2/4}\right), \quad (14)$$

$$\frac{U_{i,j}^{n+1} - U_{i,j}^{n+3/4}}{\Delta t} = S_p\left(U_{i,j}^{n+3/4}\right). \quad (15)$$

Using discretized equations,

$$U_{i,j}^{n+1} = U_{i,j}^{n} + \Delta t[S_f\left(U_{i,j}^{n+2/4}\right) + S_s\left(U_{i,j}^{n+2/4}\right) + S_p\left(U_{i,j}^{n+3/4}\right)] \quad (16)$$

$$-\frac{\Delta t}{\Delta x}[F_{i+1/2,j}^{n} - F_{i-1/2,j}^{n}] - \frac{\Delta t}{\Delta y}[G_{i+1/2,j}^{n+1/4} - G_{i-1/2,j}^{n+1/4}].$$

2.3 Integration of Topography

The decomposition method is inadequate for modelling steady-state conditions in topographical settings, as it assumes a homogeneous system. In such cases, equilibrium occurs when horizontal velocity is zero, and the pressure gradient balances the gravitational slope force. To simplify computation and maintain stability, it is assumed that elevation remains

constant in the y-direction, i.e., $\frac{\partial Z}{\partial y} = 0$. Under this assumption, the total water level is defined as $H = h + Z$, representing the system's equilibrium (Chow et al., 1988; Elong et al., 2022).

2.3.1 Water Depth at Cell Interfaces

The water depth (h) on either side of each cell interface is computed as follows to maintain numerical stability and prevent negative water depths, particularly in areas with significant bed-elevation changes (Chow et al., 1988; Elong et al., 2022).

$$h_{i+\frac{1}{2}L} = max(h_i + Z_i - max(Z_i, Z_{i+1}), 0), \tag{17}$$

$$h_{i+\frac{1}{2}R} = max(h_{i+1} + Z_{i+1} - max(Z_i, Z_{i+1}), 0). \tag{18}$$

2.3.2 State Vectors at Cell Interfaces

State vectors U in the shallow water equations represent water depth and momentum. Defined on both sides of each cell interface, these vectors capture flow variation. The numerical scheme updates U_i over time by balancing fluxes and source terms like bed slope and friction, enabling accurate flow modelling over complex terrain (Coulibaly et al., 2020; Elong et al., 2022).

$$U_{i+\frac{1}{2}L} = \left(h_{i+\frac{1}{2}L}, h_{i+\frac{1}{2}L}u_i\right) \; and \; U_{i+\frac{1}{2}R} = \left(h_{i+\frac{1}{2}R}, \; h_{i+\frac{1}{2}R}u_{i+1}\right), \tag{19}$$

$$U_i^{n+1} - U_i^n + \frac{\Delta t}{\Delta x}\left(F^n_{i+\frac{1}{2}L} - F^n_{i-\frac{1}{2}R}\right) = 0. \tag{20}$$

Where:

$$F^n_{i-\frac{1}{2}R} = F^n_{i-\frac{1}{2}L} + S^n_{i-\frac{1}{2}R} \quad and \quad F^n_{i+\frac{1}{2}L} = F^n_{i+\frac{1}{2}R} + S^n_{i+\frac{1}{2}L}, \tag{21}$$

$$S^n_{i-\frac{1}{2}R} = \left(0, P_s(h_i^n) - P_s\left(h^n_{i-\frac{1}{2}L}\right)\right) and \quad S^n_{i+\frac{1}{2}L} = \left(0, P_s(h_i^n) - P_s\left(h^n_{i+\frac{1}{2}L}\right)\right). \tag{22}$$

The pressure differences across interfaces, influenced by terrain variations, are essential components of the source term in the momentum equations, ensuring accurate modelling of flow dynamics (Coulibaly et al., 2020; Elong et al., 2022).

2.4 Integration of Rainfall Intensity

The integration on the left-hand side represents the temporal change in water depth, while the right-hand side describes the rainfall $P(h)$ minus the infiltration $I(t)$, indicating how much water is actually available to contribute to water depth change during the time steps (Coulibaly et al., 2020; Elong et al., 2022).

$$\int_{x_{i-\frac{1}{2}}}^{x_{i+\frac{1}{2}}} \int_{t^n}^{t^{n+1}} \left(\frac{\partial h}{\partial t}\right) dxdt = \int_{x_{i-\frac{1}{2}}}^{x_{i+\frac{1}{2}}} \int_{t^n}^{t^{n+1}} \big(P(h) - I(t)\big) dxdt. \tag{23}$$

By integrating Equation (23) over the half time step $[t^n, t^{n+1/2}]$, assuming constant rainfall intensity within this interval, and approximating infiltration over the same interval, the following discrete update in Equation (24) for water depth is obtained.

$$h_i^{n+\frac{1}{2}} = h_i^n + \frac{\Delta t}{2} p_i^n - \left(I\left(t^{n+\frac{1}{2}}\right) - I(t^n) \right). \tag{24}$$

The Horton model is commonly used to describe infiltration behaviour. However, it has limitations due to the variability of rainfall and infiltration parameters across different regions (Chow et al., 1988; Elong et al., 2022). The amount of water available for infiltration on a cell at time t^n is given as W_i^n:

$$W_i^n = \frac{2}{dt} h_i^n + p_i^n. \tag{25}$$

2.4.1 Determination of Infiltration

The infiltration $I_i^{n+1/2}$ is updated based on the availability of water (W) compared to the infiltration capacity $\big(I(t)\big)$. Two cases are considered. If $W \leq I(t)$, water depth is set to zero, namely, $h_i^{n+\frac{1}{2}} = 0$. If $W > I(t)$, the water depth is computed as follows (Chow et al., 1988; Elong et al., 2022):

$$h_i^{n+\frac{1}{2}} = h_i^n + \frac{\Delta t}{2} p_i^n - \left(i_f t^n + \frac{(i_0 - i_f)\left(1 - e^{-r t^n}\right)}{r} \right). \tag{26}$$

Here i_0 is the initial infiltration capacity, i_f is the final infiltration capacity, and r is the decay constant controlling the rate of decrease of infiltration capacity over time.

2.5 Numerical Flux Computation

The Harten–Lax–van Leer (HLL) scheme is a robust and efficient approximate Riemann solver for hyperbolic partial differential equations, including shallow water systems with rapidly varying flows and discontinuities. The numerical flux in the x-direction is calculated below, while the y-direction flux is obtained using the same procedure (Klingenberg et al., 2020).

2.5.1 F Flux Computations

The Jacobian matrix associated with the F-flux is given by:

$$A = \frac{\partial}{\partial U}\left[hu, hu^2 + \frac{1}{2} g h^2, huv \right]. \tag{27}$$

The eigenvalues of the Jacobian A are:

$$\beta_1^x = u - \sqrt{gh} \quad , \quad \beta_2^x = u \quad and \quad \beta_3^x = u + \sqrt{gh}. \tag{28}$$

Here, h is the water depth; g is the gravitational acceleration; u and v are the averaged velocity components in the x and y directions (Coulibaly et al., 2020).

These eigenvalues are used to determine the minimum and maximum HLL wave speeds. The coefficients C_1^x and C_2^x are calculated as:

$$C_1^x = \min_{U=U_L,U_R}\left(\min_{j=1,2,3}\beta_j^x(U)\right) \quad and \quad C_2^x = \max_{U=U_L,U_R}\left(\max_{j=1,2,3}\beta_j^x(U)\right). \tag{29}$$

Where U_L and U_R are, respectively, the left and right approximations of the solution in the cell (Coulibaly et al., 2020).

- Case 1: $0 \leq C_1^x$
  If all characteristic speeds are positive, information enters the interface from the left state and the numerical flux is $F(U_L)$.

- Case 2: $C_1^x < 0 < C_2^x$
  If the wave fan crosses the interface, the HLL intermediate flux is used. The flux is computed as a weighted combination of $F(U_L)$, $F(U_R)$, and the difference $U_L - U_R$

$$\frac{[C_2^x F(U_L) - C_1^x F(U_R) + C_1^x C_2^x (U_R - U_L)]}{[C_2^x - C_1^x]}. \tag{30}$$

- Case 3: $C_2^x \leq 0$
  If all characteristic speeds are negative, information enters the interface from the right state and the numerical flux is $F(U_R)$.

2.6 Computational Grid and Boundary Treatment Using Ghost Cells

A structured computational grid was used to discretize the study domain, with numerical calculations performed over discrete cells defined by indices i = 1, …, M and j = 1, …, N in the x- and y-directions (Elong et al., 2022; LeVeque & George, 2004). To impose boundary conditions at the edges of the domain, auxiliary cells were introduced outside the physical grid. These auxiliary cells, commonly referred to as ghost cells in numerical methods literature, are assigned values from adjacent interior cells or boundary relations so that numerical fluxes can be computed accurately and consistently at the domain boundaries.

For the x-direction boundaries:

$$U_{-1,j}^{n+1} = U_{0,j}^{n+1} = U_{1/2,j} \quad and \quad U_{M+1,j}^{n+1} = U_{M+2,j}^{n+1} = U_{M+1/2,j}. \tag{31}$$

For the y-direction boundaries:

$$U_{i,-1}^{n+1} = U_{i,0}^{n+1} = U_{i,1/2} \quad and \quad U_{i,N+1}^{n+1} = U_{i,N+2}^{n+1} = U_{i,N+1/2}. \tag{32}$$

Figure 1 illustrates the structured computational mesh and the indexing of neighboring cells used in the finite-volume discretization.

IDRiM (2026) 16 (2) **ISSN: 2185-8322**
DOI10.5595/001c.173262

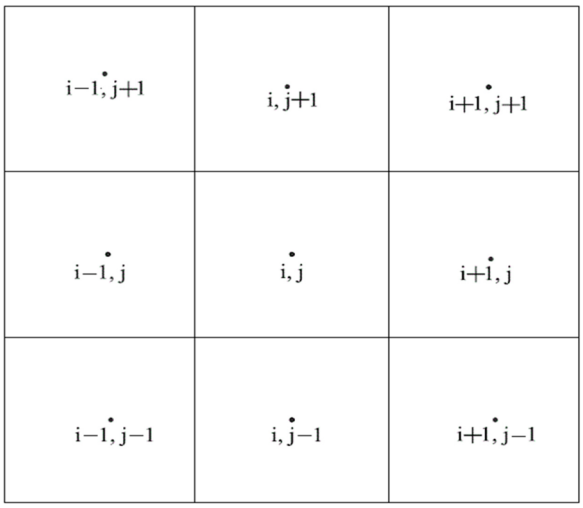

Figure 1. The Structured Mesh

Following the hydrodynamic simulations, the Flood Inundation Calculator plugin in QGIS was used as a post-processing and spatial analysis tool to convert the simulated inundation outputs into flood-risk zones and to identify relatively lower-risk areas within the Hanwella region.

3. DESCRIPTION OF STUDY AREA

Hanwella, located along the Kelani River in Sri Lanka, experiences frequent flooding due to intense rainfall and river overflow, particularly during the Southwest Monsoon and Second Inter-Monsoon periods. Upstream rainfall and rapid urbanization further worsen flood conditions by increasing surface runoff and reducing natural drainage (Manawadu & Wijeratne, 2021). Figure 2 represents the study area, Hanwella (No. 1), which receives upstream hydrological inputs from Glencourse (No. 2) and includes key sub-catchments such as Kithulgala, Deraniyagala, and Holombuwa (Nos. 3–5). Since Hanwella forms part of the wider Kelani River basin, its flood behaviour is influenced not only by local rainfall but also by upstream hydrological inputs, catchment morphology, and land-use change. Previous studies have shown that several stations in the basin, including Kithulgala, Holombuwa, Glencourse, and Hanwella, exhibit increasing precipitation and changing flood characteristics, while conversion of natural land cover to built-up areas has increased runoff generation across the basin (Samarasinghe, Makumbura, et al., 2022). This broader basin-scale setting highlights the importance of upstream runoff propagation and floodplain sensitivity in shaping flood behaviour in Hanwella (Irrigation Department, 2016).

The Kelani River basin within the Colombo District is highlighted in Figure 3.

Figure 4 highlights the Hanwella study area in red. The full extent of the Digital Elevation Model (DEM) is shown in Figure 5, while Figure 6 displays the DEM clipped to the study boundaries, providing a detailed view of the Hanwella region.

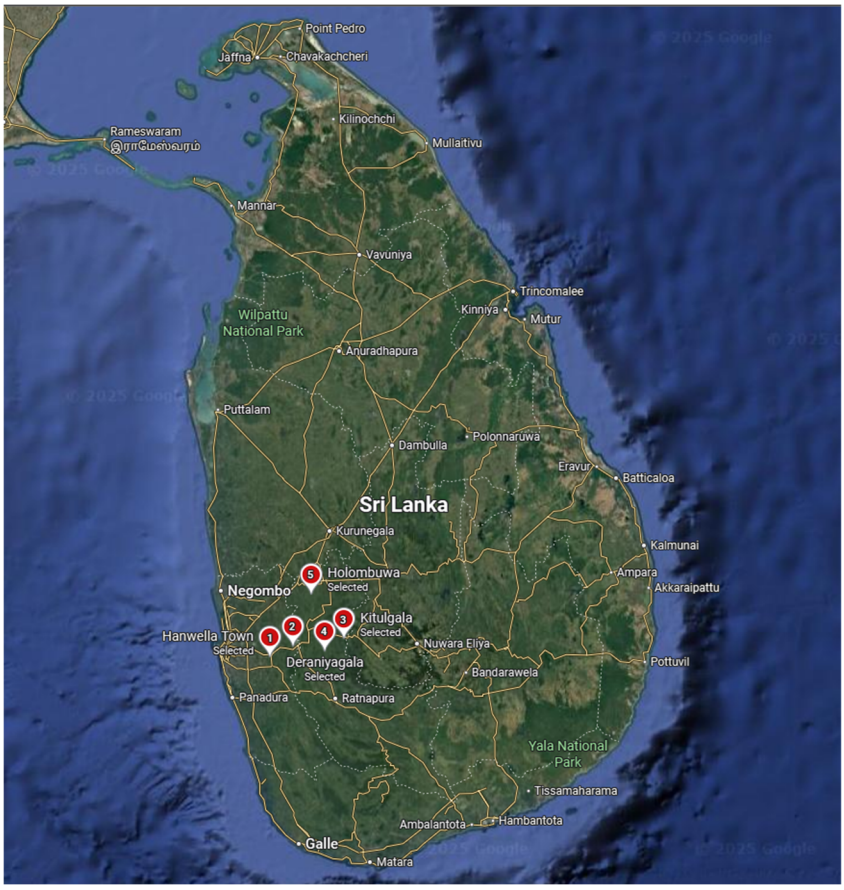

Figure 2. Location of study area and upstream

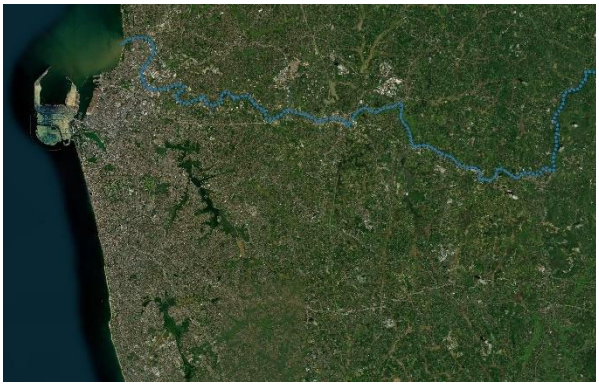

Figure 3. Kelani River in Colombo District

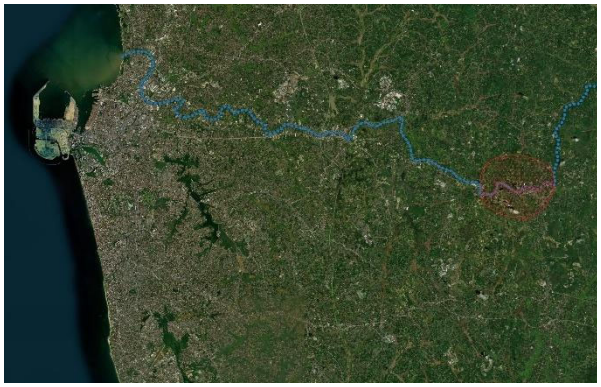

Figure 4. Location of study area Hanwella

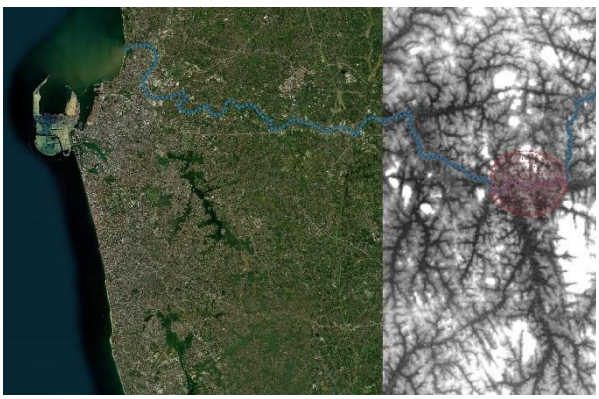

Figure 5. DEM in study area

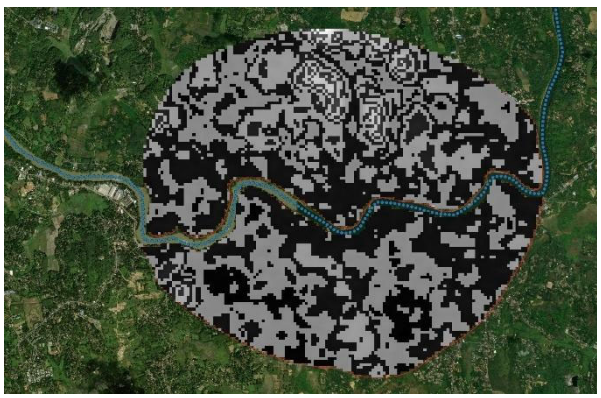

Figure 6. DEM clipped to study area

IDRiM (2026) 16 (2)
DOI10.5595/001c.173262 ISSN: 2185-8322

4. RESULTS AND DISCUSSION

4.1 Analysis of Flood Risk Levels

Figure 7 presents data from the Irrigation Department of Sri Lanka, depicting water level and rainfall conditions in the study area on 02 June 2024. The figure highlights the alert, minor flood, and major flood levels, along with relevant remarks and the trend in water levels (rising or falling). For instance, in Hanwella, the alert, minor flood, and major flood thresholds are 7.00 m, 8.00 m, and 10.00 m, respectively.

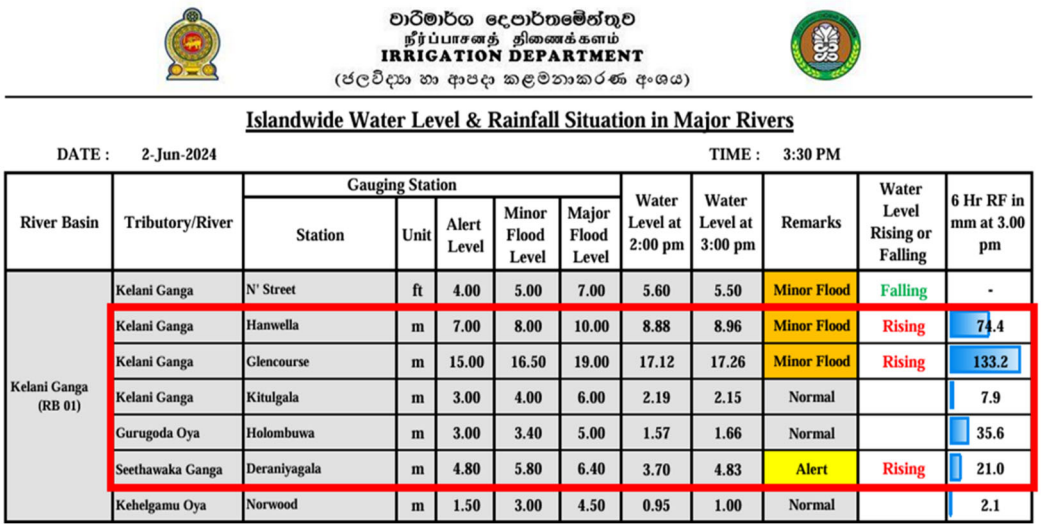

වාරිමාර්ග දෙපාර්තමේන්තුව
நீர்ப்பாசனத் திணைக்களம்
IRRIGATION DEPARTMENT
(ජලවිද්‍යා හා ආපදා කළමනාකරණ අංශය)

Islandwide Water Level & Rainfall Situation in Major Rivers

DATE : 2-Jun-2024 TIME : 3:30 PM

River Basin	Tributory/River	Gauging Station					Water Level at 2:00 pm	Water Level at 3:00 pm	Remarks	Water Level Rising or Falling	6 Hr RF in mm at 3.00 pm
		Station	Unit	Alert Level	Minor Flood Level	Major Flood Level					
Kelani Ganga (RB 01)	Kelani Ganga	N' Street	ft	4.00	5.00	7.00	5.60	5.50	Minor Flood	Falling	-
	Kelani Ganga	Hanwella	m	7.00	8.00	10.00	8.88	8.96	Minor Flood	Rising	74.4
	Kelani Ganga	Glencourse	m	15.00	16.50	19.00	17.12	17.26	Minor Flood	Rising	133.2
	Kelani Ganga	Kitulgala	m	3.00	4.00	6.00	2.19	2.15	Normal		7.9
	Gurugoda Oya	Holombuwa	m	3.00	3.40	5.00	1.57	1.66	Normal		35.6
	Seethawaka Ganga	Deraniyagala	m	4.80	5.80	6.40	3.70	4.83	Alert	Rising	21.0
	Kehelgamu Oya	Norwood	m	1.50	3.00	4.50	0.95	1.00	Normal		2.1

Figure 7. Water levels at gauging stations along the Kelani River

Table 1 presents a comparison between real and generated water levels recorded from May 1, 2024, to May 15, 2024. This example illustrates typical conditions following a minor flood event, where water levels return to normal as rainfall stabilizes.

Table 1. Comparison of real and generated water levels from May 1 to 15, 2024

Real Water Level	Remarks (Real)	Generated Water Level	Remarks (Generated)
5.00	Normal	5.68	Normal
9.10	Minor Flood	9.61	Minor Flood
9.43	Minor Flood	9.49	Minor Flood
7.95	Alert	8.95	Minor Flood
6.30	Normal	6.44	Normal
4.83	Normal	5.40	Normal
3.89	Normal	4.81	Normal
3.62	Normal	4.33	Normal
4.23	Normal	4.69	Normal
4.31	Normal	4.19	Normal
3.46	Normal	3.89	Normal
3.02	Normal	3.56	Normal
2.85	Normal	3.54	Normal
2.48	Normal	2.45	Normal
2.21	Normal	2.64	Normal

Table 2 presents a comparison between real and generated water levels recorded from April 15, 2016, to April 30, 2016. This example illustrates the typical conditions during a major flood event, characterized by 5–6 days of heavy rainfall, followed by a gradual return to near-normal water levels.

Table 2. Comparison of real and generated water levels from April 15 to 30, 2016

Real Water Level	Remarks (Real)	Generated Water Level	Remarks (Generated)
4.75	Normal	5.37	Normal
9.57	Minor Flood	10.57	Major Flood
10.41	Major Flood	10.95	Major Flood
10.53	Major Flood	11.38	Major Flood
9.65	Minor Flood	10.31	Major Flood
9.62	Minor Flood	10.12	Major Flood
8.58	Minor Flood	9.19	Minor Flood
7.21	Alert	7.11	Alert
5.76	Normal	6.89	Normal
4.97	Normal	5.99	Normal
4.84	Normal	5.90	Normal
4.61	Normal	5.59	Normal
4.74	Normal	5.16	Normal
6.61	Normal	7.05	Alert
5.66	Normal	6.09	Normal

4.2 NSE Score and Reliability of the Model

As explained in Subsection 4.1, the model generates daily water levels for the period from January 2000 to October 2024. The performance of the model was assessed by comparing simulated water levels with observed water level records using the Nash–Sutcliffe Efficiency (NSE) coefficient, rather than by comparison with another numerical model. The calculated NSE value was 0.7, indicating acceptable agreement between simulated and observed data, and all water-level values were rounded to two decimal places. The NSE, originally developed by Nash and Sutcliffe (1970), is a normalized statistic used to evaluate the relative magnitude of the residual variance compared with the variance of the observed data (Duc & Sawada, 2023). It effectively indicates how well the plot of observed versus simulated data fits the 1:1 line. The NSE is defined as follows:

$$NSE = 1 - \frac{\sum_{i=1}^{n}\left(H_i^{obs} - H_i^{sim}\right)^2}{\sum_{i=1}^{n}\left(H_i^{obs} - H^{-obs}\right)^2} \tag{33}$$

Where H_i^{obs} is the observed water depth obtained at time i, H_i^{sim} is the simulated water depth at time i, and the average observed water depth is represented by H^{-obs}.

4.3 Validation Residual Analysis and Qualitative Uncertainty Discussion

Although the model achieved an acceptable overall NSE value, discrepancies remain between the observed and simulated water levels. To characterize these discrepancies, residual-

based validation statistics were calculated using the observed and simulated values reported in Tables 1 and 2. The indicators considered were mean absolute error (MAE), root mean square error (RMSE), mean bias, and event-level Nash–Sutcliffe Efficiency (NSE). These statistics evaluate model performance at the adopted calibrated parameter set. They do not quantify sensitivity to parameter variation, boundary-condition uncertainty, calibration uncertainty, equifinality, or probabilistic uncertainty propagation.

$$MAE = \frac{1}{n}\sum_{i=1}^{n}\left|H_i^{sim} - H_i^{obs}\right|. \tag{34}$$

$$RMSE = \sqrt{\frac{1}{n}\sum_{i=1}^{n}\left(H_i^{sim} - H_i^{obs}\right)^2}. \tag{35}$$

$$Bias = \frac{1}{n}\sum_{i=1}^{n}\left(H_i^{sim} - H_i^{obs}\right). \tag{36}$$

Here, H_i^{obs} and H_i^{sim} denote the observed and simulated water levels, respectively, and n is the number of validation observations. The resulting event-level residual statistics are summarized in Table 3.

Table 3. Event-level residual-based validation statistics for observed and simulated water levels

Validation event	MAE / m	RMSE / m	Mean bias / m	Event NSE
May 1-15, 2024 minor-flood recovery event	0.49	0.56	+0.47	0.94
April 15-30, 2016 major-flood event	0.69	0.75	+0.68	0.89
Combined validation subset	0.59	0.66	+0.57	0.93

The positive mean bias indicates that the model slightly overestimates water levels in the two validation subsets. These residual statistics describe the agreement between observed and simulated values but should not be interpreted as a formal parameter-sensitivity or uncertainty-propagation analysis. From a flood-risk planning perspective, this behaviour is conservative because it reduces the likelihood of underestimating flood hazard. However, it also means that the boundaries of the mapped low-risk zones should not be interpreted as exact cadastral-scale boundaries. Instead, they should be treated as planning-scale candidate zones that require further field verification, drainage-capacity assessment, and local planning review before implementation.

Table 4 provides a qualitative, expert-based identification of model components that may influence the simulated flood behaviour. The listed effects were not obtained from parameter-perturbation experiments, boundary-condition sensitivity tests, calibration-confidence estimation, equifinality analysis, Monte Carlo simulation, or probabilistic uncertainty propagation. Therefore, the table should be interpreted only as a qualitative discussion of potential uncertainty sources. The identified urbanization-safe zones consequently represent relatively low-flood-susceptibility areas under the adopted model configuration rather than probabilistically verified or absolutely flood-free areas.

Table 4. Qualitative identification of potential model uncertainty sources

Source of uncertainty	Model component affected	Expected influence on result	Planning interpretation
Rainfall intensity uncertainty	Rainfall input R	Changes runoff volume, water depth, and inundation extent	Strong effect under moderate and high rainfall scenarios
Manning's roughness uncertainty	n_m	Changes flow velocity and local water-level attenuation	Higher roughness may increase local water depth
Curve Number/infiltration uncertainty	$CN, S,$ and infiltration terms	Changes direct runoff generation	Higher CN generally increases runoff and flood extent
DEM/topographic uncertainty	Bed elevation Z	Affects flow routing and identification of low-lying flood pockets	Important in flat floodplain areas
Upstream inflow uncertainty	Q_{inflow}	Affects river-stage contribution from upstream catchments	Important during basin-wide rainfall events

4.4 Model Response to Rainfall-Intensity Scenarios

Flood response of the Hanwella region varies across rainfall scenarios because inundation is governed not only by rainfall magnitude, but also by upstream hydrology, catchment morphology, and land-use change within the lower Kelani basin. The upper Kelani catchment receives high rainfall and has steep terrain, which promotes rapid runoff generation and routing toward the lower basin. According to the Irrigation Department (2016), the floodplain begins below the Glencourse gorge and widens downstream of Hanwella due to flatter terrain, allowing floodwaters to spread laterally once channel capacity is exceeded. As a result, prolonged basin-wide rainfall can sustain high river stages through synchronized upstream contributions, while intense rainfall can trigger rapid local flooding where infiltration and drainage are limited. Land-use change has further increased flood sensitivity by expanding built-up areas and reducing natural land cover, thereby increasing runoff generation. Samarasinghe, Makumbura, et al. (2022) reported changing precipitation characteristics at stations such as Kithulgala, Holombuwa, Glencourse, and Hanwella, together with land-use/land-cover change across the basin. This is consistent with planning evidence identifying Hanwella as highly flood-prone and in need of drainage improvement, suggesting that urban growth has intensified local flood vulnerability (Urban Development Authority, 2019). Census and local administrative data also indicate continued settlement concentration in Hanwella-related GN divisions, increasing pressure on drainage corridors and exposure in low-lying areas (Department of Census and Statistics, 2025). Therefore, differences across rainfall scenarios should be interpreted as the combined outcome of hydro-climatic forcing, basin morphology, and human modification of the landscape.

Flood extent increased nonlinearly with rainfall intensity across the simulated scenarios. Under low rainfall conditions (10–20 mm/day), inundation remained localized because the system was still able to accommodate most incoming water. Under moderate rainfall (60–75

mm/day), floodplain activation became more pronounced, leading to greater flood depth and spatial expansion. Under high rainfall conditions (150–200 mm/day), runoff increased sharply and produced substantial lateral inundation across the study area. This nonlinear pattern reflects threshold behaviour in the hydrological and hydraulic response of the Kelani River system, where relatively small increases in rainfall can produce disproportionately larger increases in flood extent once storage, conveyance, and floodplain limits are exceeded.

4.4.1 Low Rainfall Scenario

This scenario represents hydrological conditions during low rainfall periods, such as the dry season or light drizzles, with rainfall ranging from 10–20 mm/day. As shown in Figures 8 and 9, the resulting flood extent is minimal, affecting only limited areas.

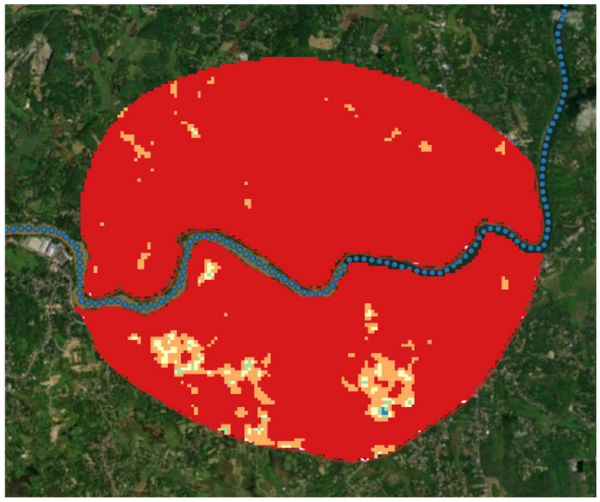

Figure 8. 15 mm/day rainfall

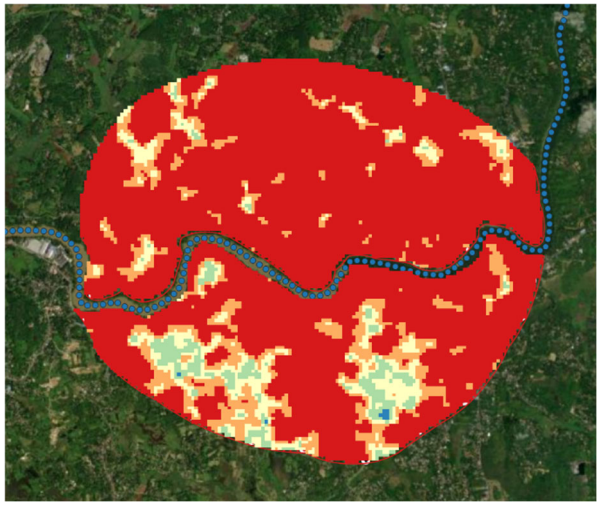

Figure 9. 20 mm/day rainfall

4.4.2 Moderate Rainfall Scenario

This scenario reflects typical hydrological conditions under moderate rainfall (60–75 mm/day), combining river base flow with average surface runoff. The resulting flood extents are shown in Figures 10 and 11.

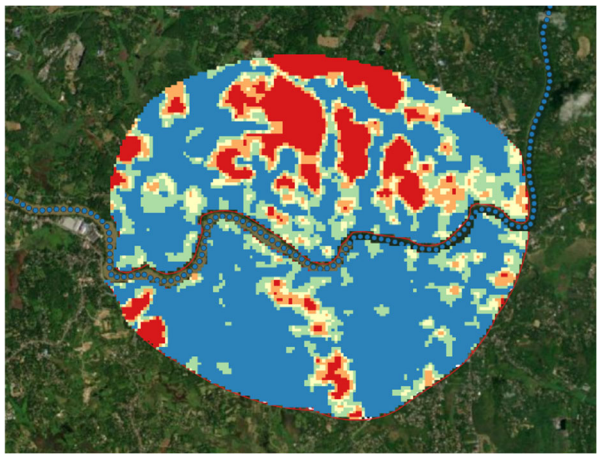

Figure 10. 60 mm/day rainfall

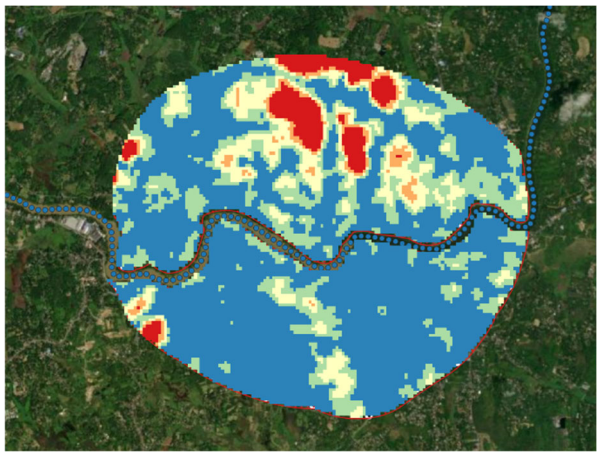

Figure 11. 70 mm/day rainfall

 ISSN: 2185-8322

4.4.3 High Rainfall Scenario

This scenario represents hydrological conditions during extreme rainfall events, characterized by high-intensity rainfall ranging from 150 to 200 mm/day. Figures 12 and 13 show the extensive flood zones triggered by intense rainfall.

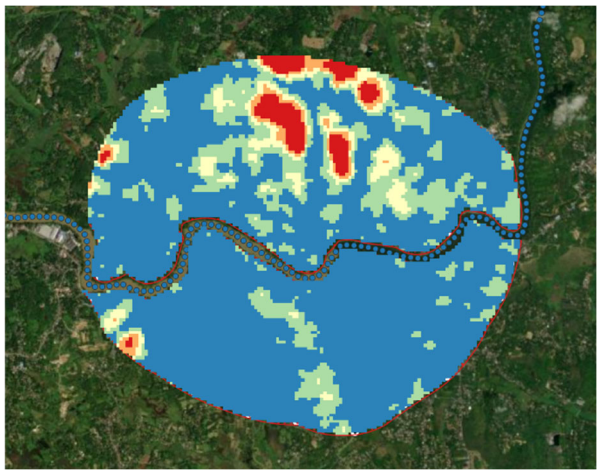

Figure 12. 150 mm/day rainfall

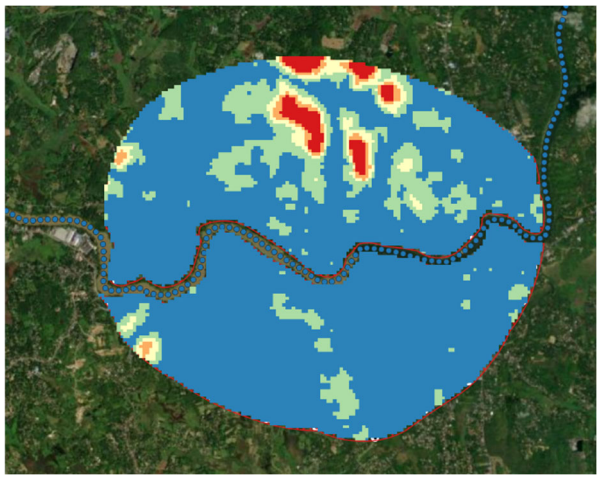

Figure 13. 190 mm/day rainfall

The scenario-response analysis shows that flood response is not uniform across rainfall ranges. The results show that in the low rainfall regime, increments of 1 mm/day produce little visible change, while increases of about 5 mm/day begin to produce noticeable differences in flood extent. Under moderate rainfall, clearer changes appear at around 10 mm/day, indicating progressive floodplain activation. In the high rainfall regime, visible differences emerge only at increments of about 20 mm/day, suggesting that once the system is already under high hydrological stress, larger increases are needed to produce distinctly new inundation patterns. Overall, these results indicate that flood behaviour in Hanwella is nonlinear and threshold-dependent, with the rainfall increment required to produce observable change increasing with rainfall intensity.

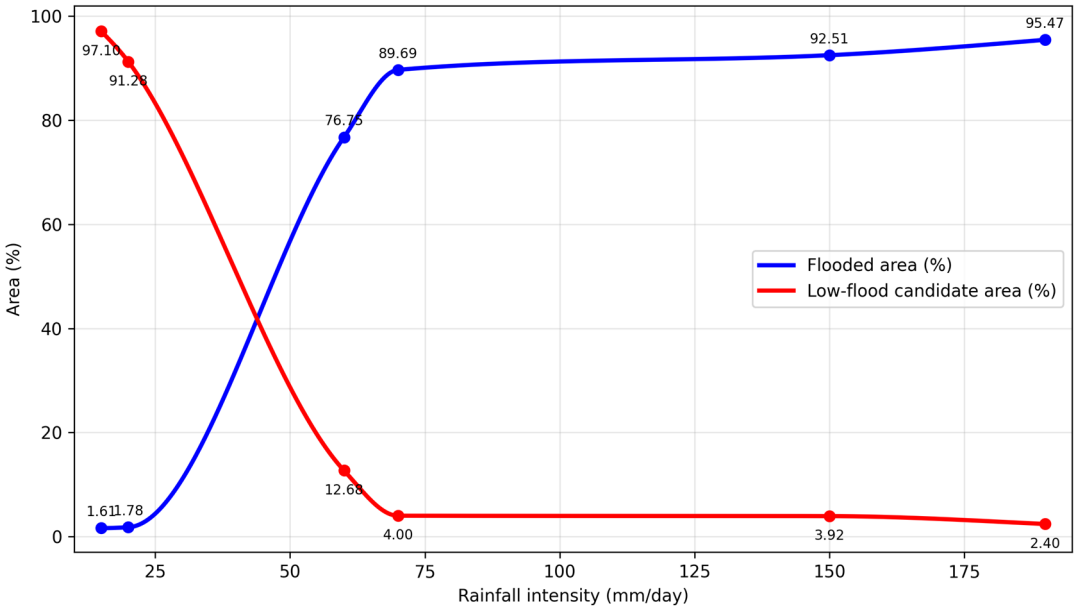

Figure 14. Variation of flooded area and low-flood candidate-zone area with rainfall intensity

Figure 14 above was therefore constructed using the original scenario maps to illustrate more clearly how the classified area changes with rainfall intensity. In the figure, the blue line represents the percentage of flooded area, while the red line represents the percentage of relatively low-flood candidate zones. As rainfall intensity increases, the flooded area increases, whereas the candidate-zone area decreases.

The opposite trends of flooded area and low-flood candidate-zone area provide a quantitative indication of how rainfall intensity affects planning-zone classification. The estimated area distribution for each rainfall-intensity scenario is summarized in Table 5.

Table 5. Estimated flood-risk area distribution under different rainfall-intensity scenarios

Rainfall intensity (mm/day)	Flooded area (%)	Transitional/moderate area (%)	Low-flood candidate area (%)
15	1.61	1.29	97.10
20	1.78	6.94	91.28
60	76.75	10.57	12.68
70	89.69	6.31	4.00
150	92.51	3.57	3.92
190	95.47	2.13	2.40

Note: The transitional/moderate area was calculated as the remaining area after subtracting the flooded area and low-flood candidate area from 100%. The interval-based changes in flooded and low-flood candidate areas are summarized in Table 6.

Table 6. Scenario-response analysis based on rainfall-intensity intervals

Rainfall interval (mm/day)	Change in flooded area (%)	Change in low-flood candidate area (%)	Response magnitude
15–20	+0.17	−5.82	Very Low
20–60	+74.97	−78.60	Very High
60–70	+12.94	−8.68	High
70–150	+2.82	−0.08	Low
150–190	+2.96	−1.52	Low

The rainfall-intensity scenario-response results show a strongly nonlinear flood response in the Hanwella region. Under low rainfall conditions, increasing rainfall from 15 mm/day to 20 mm/day produces only a very small increase in flooded area, from 1.61% to 1.78%. During this range, the low-flood candidate area remains dominant, decreasing from 97.10% to 91.28%. This indicates that the mapped flood extent changes only slightly in response to small rainfall increases under low-rainfall conditions.

A major threshold response occurs when rainfall intensity increases from 20 mm/day to 60 mm/day. In this interval, the flooded area increases sharply from 1.78% to 76.75%, while the low-flood candidate area decreases from 91.28% to 12.68%. This interval produces the largest change in mapped flooded area and low-flood candidate-zone area among the investigated rainfall scenarios. The result suggests that once rainfall exceeds the storage, infiltration, and conveyance capacity of the basin, flood expansion becomes rapid and spatially extensive.

A further increase from 60 mm/day to 70 mm/day also produces a strong response, with the flooded area increasing from 76.75% to 89.69%. At the same time, the low-flood candidate

area decreases from 12.68% to 4.00%. This confirms that the moderate-rainfall range is the most critical transition zone for flood-risk classification, because relatively small rainfall increases can substantially reduce the area available for safer urbanization.

Under high rainfall conditions, from 70 mm/day to 150 mm/day and from 150 mm/day to 190 mm/day, the incremental expansion of the mapped flooded area becomes smaller. The flooded area increases only slightly from 89.69% to 92.51% and then to 95.47%, while the low-flood candidate area remains very small. This indicates a saturation effect: once most of the study area is already flood-affected, additional rainfall produces only limited expansion in mapped flooded area.

Overall, the scenario-response analysis demonstrates that flood behaviour in Hanwella is threshold-dependent rather than linear. The most important transition occurs between low and moderate rainfall intensities, especially from 20 mm/day to 60 mm/day. This has important planning implications because areas identified as low-flood candidate zones under low rainfall may rapidly become unsuitable when rainfall intensity crosses the critical threshold. Therefore, urbanization-safe zones should be interpreted cautiously and considered together with the residual-based validation results, qualitative uncertainty discussion, field verification, and drainage-capacity assessment before being used for land-use planning decisions.

4.5 Numerical Results

Figure 15 presents the flood-risk zones in Hanwella based on 2D model outputs, categorized as high (blue), moderate (yellow/orange), and low-risk (red) areas. Based on these results, Figure 16 identifies relatively low-risk zones that remain less exposed across multiple rainfall scenarios and are therefore considered as flood-informed candidate zones for future urbanization. In this context, low-risk areas are interpreted as candidate development zones, whereas moderate- and high-risk areas require development control, mitigation measures, or protection-oriented planning.

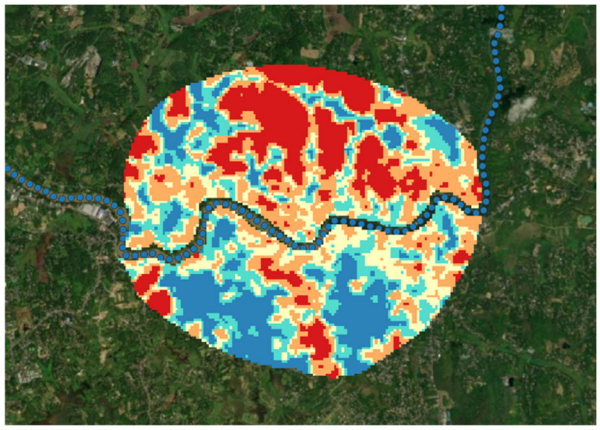

Figure 15. Flood risk map of the Hanwella area

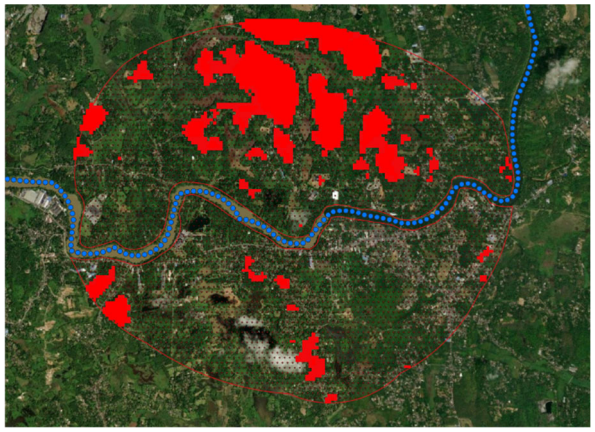

Figure 16. Areas for future urbanization

The future-urbanization candidate patches were interpreted by comparing the low-flood-risk map with the official Seethawaka ward map and GN-level settlement information (Ministry of Public Administration, Provincial Councils and Local Government, n.d.). Therefore, the

identified zones should be understood as planning-scale candidate areas rather than exact cadastral boundaries. Recent GN-level census data further indicate that these surrounding divisions already support notable resident populations, with the 2024 Census reporting Hanwella Town: 2809, Ihala Hanwella North: 1555, Diddeniya North: 1743, Ihala Hanwella South: 915, Pahathgama: 1917, Jayaweeragoda: 2153, Koodaluvila: 3253, and Thunnana East: 863, while the former Hanwella Divisional Secretariat Division recorded a population of 113807 in the 2012 Census. These values suggest that the identified lower-flood-risk areas are not isolated vacant parcels, but are linked to already inhabited settlement pockets (Department of Census and Statistics, 2012, 2025). The census counts suggest that the mapped safer areas are associated with a moderately populated peri-urban environment rather than undeveloped empty space (Department of Census and Statistics, 2025). This is also consistent with the Seethawaka Development Plan 2019–2030, which identifies the Hanwella–Waga sector as an area targeted for future residential and urban development (Urban Development Authority, 2019).

From a planning perspective, these findings support moving beyond static land classification toward a risk-informed zoning approach guided by hydrological behaviour, floodplain connectivity, and infrastructure capacity (Greiving et al., 2023). Zoning can therefore reduce exposure by directing settlement and future development away from areas subject to recurrent inundation or drainage constraints (World Bank, 2013). Previous studies likewise emphasize that effective flood-risk-based zoning should incorporate hazard intensity, vulnerability, and long-term urban growth patterns, particularly in rapidly urbanizing regions where development in low-lying land can increase both runoff and human exposure (Der Sarkissian et al., 2022; Manandhar et al., 2023). Accordingly, the identified lower-risk zones are interpreted as flood-informed candidate areas for future urban expansion, while also highlighting the need to integrate hydrodynamic results with socio-economic and infrastructure data for more comprehensive urban resilience planning (De Silva & Kawasaki, 2022; World Bank, 2023).

5. CONCLUSIONS

This study developed a two-dimensional hydrodynamic flood modelling framework for the Hanwella region based on the shallow water equations and implemented it using a Godunov-type Finite Volume Method with the Harten–Lax–van Leer (HLL) Riemann solver. The model incorporated upstream river contributions, overland flow, rainfall, infiltration, surface roughness, and topographic information to simulate flood dynamics under varying hydrological conditions. The results confirmed that flood behaviour in Hanwella is nonlinear and threshold-dependent, with flood extent increasing substantially as rainfall intensity rises and with different rainfall ranges producing different levels of floodplain response.

By integrating hydrodynamic model outputs with GIS-based spatial analysis, the study identified relatively lower-risk areas that were considered as flood-informed candidate zones for future urbanization. These findings show that the identified lower-risk areas are not simply isolated vacant land, but are associated with existing settlement environments, which increases

their relevance for planning purposes. The study therefore extends beyond flood simulation alone and provides a practical basis for risk-sensitive zoning, land-use planning, and targeted flood mitigation in the Hanwella region.

Overall, the study demonstrates that combining two-dimensional hydrodynamic modelling with GIS-based flood-risk mapping provides a scientifically grounded and practically useful framework for understanding flood behaviour and supporting safer urban development in flood-prone areas. The uncertainty treatment was confined to validation-residual statistics calculated at the adopted calibrated parameter set and a qualitative expert-based assessment of potential uncertainty sources. Formal parameter-perturbation experiments, boundary-condition sensitivity tests, calibration-uncertainty analysis, and probabilistic uncertainty propagation were not conducted and should be addressed in future work. Therefore, the mapped low-flood candidate zones should be interpreted as planning-scale evidence under the adopted model assumptions rather than as probabilistically verified or absolutely flood-free areas. Future studies should conduct a Manning's n sensitivity sweep across a defensible range of roughness values and at least one boundary-condition sensitivity test, together with calibration-confidence or equifinality analysis and Monte Carlo or other probabilistic uncertainty-propagation methods. Future work should also incorporate higher-resolution topographic data and additional event-based calibration and validation. The findings highlight the importance of moving beyond static land classification toward a flood-informed planning framework that better reflects hydrological behaviour, spatial flood patterns, and the need for more resilient urban growth in Hanwella.

REFERENCES

Barreiro, J., Santos, F., Ferreira, F., Neves, R., & Matos, J. S. (2022). Development of a 1D/2D urban flood model using the open-source models SWMM and MOHID Land. *Sustainability, 15*(1), 707. https://doi.org/10.3390/su15010707

Benedini, M., & Tsakiris, G. (2013). *Water quality modelling for rivers and streams*. Springer. https://link.springer.com/book/10.1007/978-94-007-5509-3

Brunner, G. W. (2024). *HEC-RAS 2D user's manual (Version 6.6)*. U.S. Army Corps of Engineers, Hydrologic Engineering Center. https://www.hec.usace.army.mil/confluence/rasdocs/r2dum/6.6

Caviedes-Voullième, D., Fernández-Pato, J., & Hinz, C. (2020). Performance assessment of 2D zero-inertia and shallow water models for simulating rainfall-runoff processes. *Journal of Hydrology, 584*, 124663. https://doi.org/10.1016/j.jhydrol.2020.124663

Chen, W.-B., Chang, T.-Y., Chen, H., Fu, H.-S., Yu, Y.-C., Su, W.-R., & Lin, L.-Y. (2021). An operational high-performance forecasting system for city-scale pluvial flash floods in the southwestern plain areas of Taiwan. *Water, 13*(4), 405. https://doi.org/10.3390/w13040405

Chen, Y., Wang, X., Tong, J., Liu, X., Yang, J., & Liu, X. (2022). Flood hazard zone mapping incorporating geographic information for spatial planning and flood risk management. *Journal of Hydrology, 613*. https://doi.org/10.1016/j.jhydrol.2022.128441

Chow, V. T., Maidment, D. R., & Mays, L. W. (1988). *Applied hydrology*. McGraw-Hill. https://ponce.sdsu.edu/Applied_Hydrology_Chow_1988.pdf

Costabile, P., Costanzo, C., De Lorenzo, G., & Macchione, F. (2021). A 2D-SWEs framework for efficient catchment-scale hydrodynamic-based rainfall-runoff modelling. *Journal of Hydrology, 598*, 126275. https://doi.org/10.1016/j.jhydrol.2021.126275

Coulibaly, G., Leye, B., Fowe, T., Karambiri, H., & Mounirou, L. A. (2020). Urban flood modeling using 2D shallow-water equations in Ouagadougou, Burkina Faso. *Water, 12*(8), 2120. https://doi.org/10.3390/w12082120

De Silva, M., & Kawasaki, A. (2022). Modeling the association between socioeconomic features and risk of flood damage: A local-scale case study in Sri Lanka. *International Journal of Disaster Risk Reduction*. https://doi.org/10.1111/risa.13894

Department of Census and Statistics. (2012). *Census of Population and Housing 2012*. https://www.statistics.gov.lk/Population/StaticalInformation/CPH2011

Department of Census and Statistics. (2025). *Census of Population and Housing 2024: Occupied housing units by Grama Niladhari Division (provisional)*. https://www.statistics.gov.lk/Resource/en/Population/CPH_2024/GN_housing_pdf.pdf

Der Sarkissian, R., Vranken, L., Mansourian, A., & Valizadeh Kamran, K. (2022). Land use planning to reduce flood risk: Opportunities, challenges and uncertainties in disaster risk reduction. *Sensors, 22*(18), 6957. https://doi.org/10.3390/s22186957

Duc, L., & Sawada, Y. (2023). A signal-processing-based interpretation of the Nash–Sutcliffe efficiency. https://doi.org/10.5194/hess-27-1827-2023

Elong, A. J., Zhou, L., Karney, B., Fang, H., Cao, Y., & Zeh Assam, S. L. (2022). Flood prediction with two-dimensional shallow water equations: A case study of Tongo Bassa watershed in Cameroon. *Water Journal*. https://doi.org/10.3390/app122211622

Global Facility for Disaster Reduction and Recovery. (2017). *Land use planning for urban flood risk management*. World Bank Group. https://openknowledge.worldbank.org/entities/publication/6b4f3e3a-e718-5046-a881-c1621f78f504

Greiving, S., Kruse, P., Othmer, F., Fleischhauer, M., & Fuchs, M. (2023). Implementation of risk-based approaches in urban land use planning. *Sustainability, 15*(21), 15340. https://doi.org/10.3390/su152115340

Hirabayashi, Y., Tanoue, M., Sasaki, O., Zhou, X., & Yamazaki, D. (2021). Global exposure to flooding from the new CMIP6 climate model projections. *Scientific Reports, 11*(1), 3740. https://doi.org/10.1038/s41598-021-83279-w

Iresh, A. D. S., Marasingha, A. G. N. S., Wedanda, A. M. T. S. H., Wickramasekara, G. P., Wickramasooriya, M. D. J. P., & Premathilaka, M. T. C. (2021). Development of a hydrological model for Kala Oya Basin using SWAT model. *ENGINEER, 54*(1), 57. https://doi.org/10.4038/engineer.v54i1.7435

Irrigation Department. (2016). *Hydrological annual 2015/16*. https://irrigation.gov.lk/web/images/Hydrological-Annual/9_Hydrological_Annual_2015-2016.pdf

Jongman, B., Ward, P. J., & Aerts, J. C. J. H. (2014). Global exposure to river and coastal flooding: Long-term trends and changes. *Nature Climate Change, 4*(3), 264–268. https://doi.org/10.1016/j.gloenvcha.2012.07.004

Klingenberg, C., Kurganov, A., Liu, Y., & Zenk, M. (2020). Moving-water equilibria preserving HLL-type schemes for the shallow water equations. *Journal of Scientific Computing, 85*, 1–27. https://doi.org/10.4208/cmr.2020-0013

Kurganov, A. (2018). Finite-volume schemes for shallow-water equations. *Acta Numerica, 27*, 289–351. https://doi.org/10.1017/S0962492918000028

LeVeque, R. J., & George, D. L. (2004). High-resolution finite volume methods for the shallow water equations with bathymetry and dry states. In *Proceedings of the 3rd International Symposium on Finite Volumes for Complex Applications*. https://doi.org/10.1142/9789812790910_0002

Makumbura, R. K., Gunathilake, M. B., Samarasinghe, J. T., Confesor, R., Muttil, N., & Rathnayake, U. (2022). Comparison of calibration approaches of the Soil and Water Assessment Tool (SWAT) model in a tropical watershed. *Hydrology Research*. https://doi.org/10.3390/hydrology9100183

Manandhar, B., Cui, S., Wang, L., & Shrestha, S. (2023). Urban flood hazard assessment and management practices in South Asia: A review. *Land, 12*(3), 627. https://doi.org/10.3390/land12030627

Manawadu, L., & Wijeratne, V. (2021). Anthropogenic drivers of urban flash floods in the Lower Kelani River Basin, Colombo, Sri Lanka. *International Journal of Disaster Risk Reduction*. https://doi.org/10.1016/j.ijdrr.2021.102076

Ministry of Public Administration, Provincial Councils and Local Government. (n.d.). *Ward map of Seethawaka Pradeshiya Sabha*. Government of Sri Lanka. https://mpclg.gov.lk/web/images/wardmaps/colombo/12_Colombo_SeethawakaPS_Section2.pdf

Moufar, M. M. M., & Perera, E. D. P. (2018). Floods and countermeasures impact assessment for the Metro Colombo Canal System, Sri Lanka. *Hydrology, 5*(1), 11. https://doi.org/10.3390/hydrology5010011

Nash, J. E., & Sutcliffe, J. V. (1970). River flow forecasting through conceptual models part I—A discussion of principles. *Journal of Hydrology, 10*(3), 282–290. https://doi.org/10.1016/0022-1694(70)90255-6

Perera, T. A. N. T., Piyadasa, R. U. K., Gunarathna, M. H. J. P., & Kumar, D. N. (2024). SWAT model to simulate hydrological responses to land use and land cover change in the Kelani River basin, Sri Lanka. *Groundwater for Sustainable Development*. https://doi.org/10.1016/j.gsd.2024.101251

Samarasinghe, J. T., Basnayaka, V., Gunathilake, M. B., Azamathulla, H. M., & Rathnayake, U. (2022). Comparing combined 1D/2D and 2D hydraulic simulations using high-resolution topographic data: Examples from Sri Lanka—Lower Kelani River Basin. *Hydrology, 9*(2), 39. https://doi.org/10.3390/hydrology9020039

Samarasinghe, J. T., Makumbura, R. K., Wickramarachchi, C., Sirisena, J., Gunathilake, M. B., Muttil, N., Teo, F. Y., & Rathnayake, U. (2022). The assessment of climate change impacts and land-use changes on flood characteristics: The case study of the Kelani River Basin, Sri Lanka. *Hydrology, 9*(10), 177. https://doi.org/10.3390/hydrology9100177

Urban Development Authority. (2019). *Seethawaka Pradeshiya Sabha development plan 2019–2030*. https://www.uda.gov.lk/attachments/devplan_detailed/Development%20Plans%202019-2030/Seethawaka/English.pdf

U.S. Department of Agriculture. (1986). *Urban hydrology for small watersheds: Technical Release 55 (TR-55)*. Natural Resources Conservation Service. https://www.nrc.gov/docs/ML1421/ML14219A437.pdf

World Bank. (2013). *Building urban resilience: Principles, tools, and practice*. https://doi.org/10.1596/978-0-8213-8865-5

World Bank. (2023). *Technical support for integrating flood risk management into urban and spatial planning*. https://documents1.worldbank.org/curated/en/099041423111519720/pdf/P1723260e84ddd0ba08e42015b72d926423.pdf